Acta Oceanol. Sin., 2024, Vol. 43, No. 5, P. 30–40
https://doi.org/10.1007/s13131-024-2323-x
http://www.aosocean.com
E-mail: ocean2@hyxb.org.cn

Spatiotemporal features and vertical structures of four types of mesoscale eddies in the Kuroshio Extension region

Bowen Sun[1], Shuchang Xu[2], Zhankun Wang[1], Yujie Feng[1], Baofu Li[1]*

[1] School of Geography and Tourism, Qufu Normal University, Rizhao 276800, China

[2] Faculty of Information Science and Engineering, Ocean University of China, Qingdao 266100, China

Received 1 December 2023; accepted 29 February 2024

Abstract

Except for conventional mesoscale eddies, there are also abundant warm cyclonic eddies (WCEs) and cold anticyclonic eddies (CAEs) in the global ocean. Based on the global mesoscale eddy trajectory atlas product, satellite altimetric and remote sensing datasets, and three-dimensional temperature/salinity dataset, spatiotemporal features of WCEs and CAEs are compared with traditional cold cyclonic eddies and warm anticyclonic eddies in the Kuroshio Extension (KE; 28°–43°N, 140°–170°E) region. Characteristics of abnormal eddies like radius, amplitude, eddy kinetic energy, and proportion in all eddies behave in significant asymmetry on the north and south sides of the KE jet. Unlike eddies in the general sense, temporal feature analysis reveals that it is more favorable to the formation and maintenance of WCEs and CAEs in summer and autumn, while winter is the opposite. The spatiotemporal variation of abnormal eddies is likely because the marine environment varying with time and space. Statistically, proportion of abnormal eddies increases rapidly in decaying stage during the whole eddy lifespan, resulting in smaller average radius, amplitude, sea surface temperature anomaly and sea surface height anomaly compared to normal ones. The three-dimensional composite structures for four types of eddies expose that the difference between abnormal and conventional eddies is not just limited to the sea surface, but also exists within the water below the sea surface. Vertical structures also indicate that the anomalous temperature signal is confined in the water from the sea surface to layers at about 30 m in the KE region.

Citation: Sun Bowen, Xu Shuchang, Wang Zhankun, Feng Yujie, Li Baofu. 2024. Spatiotemporal features and vertical structures of four types of mesoscale eddies in the Kuroshio Extension region. Acta Oceanologica Sinica, 43(5): 30–40, doi: 10.1007/s13131-024-2323-x

1 Introduction

Mesoscale oceanic eddies reserve a huge amount of energy and play an important role in material and energy transport and air-sea interaction (Dong et al., 2017; Sun et al., 2019b; Yang et al., 2023). Conventionally, a cyclonic eddy (CE)/an anticyclonic eddy (AE) appears a quasi-monopolar cold-core/warm-core sea surface temperature (SST) pattern, under the combined action of the vertical pumping and lateral swirling (Frenger et al., 2015; Gaube et al., 2015; Sun et al., 2019b; Yu et al., 2021; Lv et al., 2022). Recent studies reveal that there are a certain proportion of warm cyclonic eddies (WCEs) and cold anticyclonic eddies (CAEs), which are also named as abnormal eddies (Sun et al., 2019a; Liu et al., 2021). Since negative/positive SST anomaly induced by CEs/AEs can impact local atmospheric parameters like wind speed, clouds, and precipitation in marine atmosphere boundary layer overlying them differently (Ma et al., 2015; Renault et al., 2019; Sun et al., 2020, 2022; Desbiolles et al., 2021), there will be certain errors if ignoring the existence of abnormal eddies when discussing issues like air-sea interaction or heat flux associated with oceanic mesoscale eddies (Xu et al., 2018; Ni et al., 2021). In addition, some studies on oceanic mesoscale eddies conducted eddy identification methods based on SST derived from *in situ* observation or infrared imagery (Castellani, 2006; Fernandes and Nascimento, 2006; D'Alimonte, 2009; Ji et al., 2017). To a certain extent, the existence of abnormal eddies could lead to confusion in the determination of eddy polarity.

The WCEs and CAEs are usually fewer in occurrence number than eddies with traditional SST anomaly features, which are mentioned as cold cyclonic eddies (CCEs) and warm anticyclonic eddies (WAEs) hereinafter. Early studies were mostly based on monitoring conductivity, temperature and depth (CTD) and shipborne acoustic Doppler current profiler (ADCP) data to explore individual cases of abnormal eddies in the subarctic area (Mathis et al., 2007; Itoh and Yasuda, 2010a, 2010b). Along with the wide application of satellite altimetry data and remote sensing SST data, researchers can identify a large number of mesoscale eddies and select abnormal eddy signals according to certain criteria, making carrying out statistical analysis on spatiotemporal characteristics of abnormal eddies in global ocean to be practical. Several regional studies reveal the high percentage of abnormal eddies in the areas like the South China Sea (Sun et al., 2021), the Tasman Sea (Everett et al., 2012), the North Pacific Ocean (Sun et al., 2019a) and the tropical oceans (Ni et al., 2023). It is affirmed that the WCEs and CAEs are rather abundant in the global ocean (Ni et al., 2021), especially in areas associated with the Equatorial Current and regions between the continental shelves and high unstable currents like the Oyashio Current, western boundary currents, and Antarctic Circular Current (Liu et al., 2021). In terms of the temporal characteristics, the existence number and occurrence frequency for WCEs and CAEs in

---

Foundation item: The Natural Science Foundation of Shandong Province under contract No. ZR2021YQ28; the Taishan Scholars Project of Shandong Province under contract No. tsqn202306182.

*Corresponding author, E-mail: libf@qfnu.edu.cn

the North Pacific are highest in summer and lowest in winter (Sun et al., 2019a; Liu et al., 2021). The statistics show that the abnormal eddy signals usually generate in the beginning stage and the decaying stage of eddy (Sun et al., 2019a). The study also verified two types of formation mechanisms for the abnormal eddies through the case study on the evolution process of an eddy case. The increased instability of the studied CE led to a fast enlarged radius and absorption of warm water from the surrounding environment in its decaying stage, which finally resulted in the transition of the normal CE into a WCE. The studied AE was turned into a CAE because of the eddy-current interaction.

The area associated with the Kuroshio Extension (KE, 28°–43°N, 140°–170°E) has the highest eddy kinetic energy (EKE) in the North Pacific because the KE sheds off numerous mesoscale eddies towards its two flanks while flowing easterly (Qiu et al., 2017; Ji et al., 2018). A large number of studies have investigated the activity characteristics, structural features, and air-sea interactions of mesoscale eddies in the region (Itoh and Yasuda, 2010b; Kouketsu et al., 2016; Yang et al., 2018; Shan et al., 2020a, 2020b; Yao et al., 2023). According to the statistics in Sun et al. (2019a) and Ni et al. (2021), the KE region is also one of the regions with the highest occurrence frequency of WCEs and CAEs. At present, although several studies have conducted statistical analysis on the characteristics of WCEs and CAEs to a certain extent, there is still no clear understanding of the spatiotemporal features and general structural characteristics of these abnormal eddies.

The paper is structured as follows: The data sets, the pre-processing method, abnormal eddy definition method, and spatial structure composite method are detailed in Section 2. The spatiotemporal variation features of WCEs and CAEs in the KE region are statistically analyzed based on sea surface observational data and mesoscale eddy trajectory atlas product in Section 3. In Section 4, the spatial composite structures of the abnormal eddies and conventional eddies in the study area are constructed by using three-dimensional temperature/salinity fields, and the difference between abnormal eddies and regular eddies is further compared. Section 5 summarizes the main conclusions and discussions of this study.

2 Data and methods

2.1 *Data*

2.1.1 *AVISO Absolute Dynamic Topography (ADT) data*

The sea surface height (SSH) anomaly field in the study area is obtained from the multiple satellite-merged daily SSH data provided by the Archiving, Validation, and Interpolation of Satellite Oceanographic (AVISO) (http://www.aviso.oceanobs.com/), with a spatial resolution of 0.25° × 0.25°. The SSH anomaly (h') signal associated with mesoscale eddies is extracted from the original SSH field through pre-filtering as is presented in Zu et al. (2019). Firstly, a 3-week low-pass temporal filter is conducted to eliminate the synoptic scale disturbance in SSH. Secondly, a 52-week high-pass temporal filter is used to remove variation in time scale over years. According to the general horizontal scale in O (100 km) of oceanic mesoscale eddies, a two-dimensional spatial high-pass filter with a 4° (about 440 km) half-width was further conducted to extract signals associated with mesoscale eddies from the background fields. Taking the balance of pressure gradient force and Coriolis force approximately, the geostrophic velocity anomaly (u' and v' for zonal and meridional component, respectively) is calculated based on the mesoscale SSH anomaly field, which can be regarded as the tangential velocity around the mesoscale eddy center:

$$\begin{cases} u' = -\dfrac{g}{f}\dfrac{\partial h'}{\partial y}, \\ v' = \dfrac{g}{f}\dfrac{\partial h'}{\partial x}, \end{cases} \tag{1}$$

where g is the gravitational acceleration, $g = 9.8\ \mathrm{m/s^2}$; f is the Coriolis parameter at the corresponding latitude. The EKE is further evaluated as follows:

$$\mathrm{EKE} = \frac{1}{2}\left(u'^2 + v'^2\right). \tag{2}$$

2.1.2 *AVHRR-only-v2*

To reveal the SST anomaly structure induced by mesoscale eddies, we also use the daily SST data provided by the optimum interpolation Advanced Very High-Resolution Radiometer (AVHRR-only-v2) SST product, with a spatial resolution of 0.25° × 0.25°. The access website is https://climatedataguide.ucar.edu/climate-data/. For consistency, the SST data are pre-filtered before determining abnormal or not and compositing in the same way as SSH data to obtain mesoscale SST anomaly.

2.1.3 *Mesoscale eddy trajectory Atlas product*

A global mesoscale eddy dataset Meta3.1exp DT (Delayed-time) allsat version released by AVISO is used directly in this study. The dataset contained mesoscale eddies identified and tracked from the altimetric dataset in the global ocean during January 1993 to March 2020, including information like eddy center location, tangential speed, amplitude, and effective radius (Pegliasco et al., 2022). Eddies that last longer than 28 d located in the KE and surrounding areas during the period of January 1993 to December 2019 are selected for the analysis in this study. The eddy dataset is obtained through the website: https://data.aviso.altimetry.fr/aviso-gateway/data/META3.1exp_DT/.

It is worth noting that the selected eddy snapshots include not only eddy trajectories that exist in the study area throughout the survival cycle, but also the eddies generated outside and propagated into the study area later, and the eddies generated inside but later propagated out of the study area. Therefore, to eliminate the influence of the above different situations on determining the stage of eddy snapshot in its whole life cycle, the eddy trajectories located inside the research area from their generation to death are selected to reconstruct the evolution process during the lifetime.

2.1.4 *Three-dimensional temperature/salinity (T/S) dataset*

To recognize the exact three-dimensional structures of mesoscale eddies, the temperature and salinity data derived from the Multi Observation Global Ocean ARMOR3D L4 analysis and multi-year reprocessing dataset provided by Copernicus Marine Environment Monitoring Service (CMEMS) is used in this study. The dataset provides a weekly three-dimensional T/S field from January 1, 1993 to the present with a horizontal resolution of 0.25° × 0.25°, which is vertically divided into 50 levels (41 levels in upper 1 500 m depth). The dataset is available at https://data.

marine.copernicus.eu/product/MULTIOBS_GLO_PHY_TSUV_3D_MYNRT_015_012/services.

Firstly, the T/S field on each depth layer is filtered following the same procedures as SSH and SST data to obtain the T/S anomaly signals related to mesoscale eddies under the sea surface. Besides, the steric dynamic height anomaly H' at different levels associated with mesoscale eddies is also calculated based on the three-dimensional T/S field (Dilmahamod et al., 2018):

$$H'(S, T, P) = \int_{\text{ref-lev}}^{P} \delta\rho(S, T, P)\,\mathrm{d}p, \tag{3}$$

where S, T, and P denote the salinity, temperature, and pressure of seawater on each level, seawater density ρ is derived from the T/S field, seawater density anomaly $\delta\rho$ is further obtained by using the same filtering method as the T/S field. The reference level (ref-lev) is set to $1\ 500 \times 10^4$ Pa, which is commonly considered as no-motion by previous studies (Yang et al., 2015). Finally, the T', S', and H' fields are matched with the mesoscale eddy snapshots temporally and spatially to obtain the composite structure of the eddies. Due to the quasi-geostrophic nature of mesoscale eddies, the three-dimensional structure of geostrophic velocity (V_g) anomaly for eddies can be calculated by combining the composite H' structure with the geostrophic balance relationship, which is similar to Eq. (1).

2.2 *Methods*

2.2.1 *Definition of abnormal eddies*

WCEs and CAEs are selected from the numerous eddy snapshots in the study period and region as follows. For each eddy snapshot, the pre-filtered mesoscale SST anomaly within one radius from eddy center is selected to calculate the average value T'_{in}. If the T'_{in} of a CE snapshot is positive/negative, it is judged as a WCE/CCE. Similarly, if the T'_{in} of an AE snapshot is negative/positive, it is judged as a CAE/WAE. Another relevant indicator is γ_b, which is calculated by dividing the number of abnormal grid points inside the eddy core by the total number of grid points inside the eddy core. In different studies, the determination conditions of abnormal eddies are not consistent, which will lead to the difference in analysis results, especially the number and frequency of eddies, but will not have a substantial impact on the results of other characteristics and structures of eddies (Sun et al., 2021).

2.2.2 *Composite analysis*

In the coordinate system with eddy center and eddy normalized radius as the axis, the eddy SST, SSH, three-dimensional temperature, and dynamic height anomaly structures are composited following the method in Chaigneau et al. (2011). The resultant three-dimensional structures are interpolated vertically into equally spaced from sea surface to 1 500 m depth with an interval of 10 m.

2.2.3 *Index of abnormal eddy (IAE)*

In this study, the Pearson correlation coefficient between the composite SST anomaly (SSTA) structure and the composite SSH anomaly (SSHA) structure will be used as an index to measure the degree of the abnormality in eddy temperature structures: IAE = R (SSTA, SSHA), the value of which is in the range of –1 to 1. When the value is positive, the SST anomaly of CE/AE appears cold-core/warm-core feature, which is the most common. Conversely, if the value is negative, the SST anomaly of CE/AE appears warm-core/cold-core feature instead. Besides, the larger the absolute value of IAE is, the closer the core of SST anomaly to the eddy center is. On the contrary, the smaller the absolute value of IAE is, the more dipolar the SST anomaly pattern is. The coefficient can help quantitatively assess the degree of abnormality in the temperature structure of eddies and the degree of proximity to a monopole.

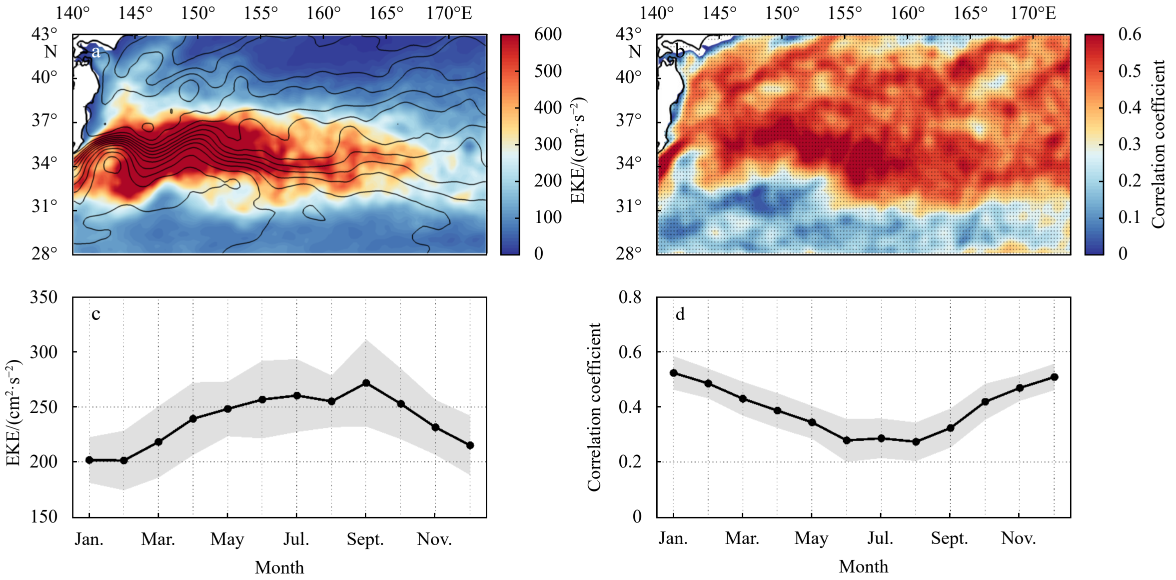

Fig. 1. Distribution of average eddy kinetic energy (EKE, shading) and absolute dynamic topography (ADT, contours) in the Kuroshio Extension jet and its vicinity (a), correlation coefficient of mesoscale sea surface height anomaly (SSHA) and sea surface temperature anomaly (SSTA) (the dotted region means passing the significance test of 0.01) (b), climatological monthly regional-average EKE (c), and annual cycle of spatial correlation coefficient of mesoscale SSHA and SSTA (d). The shadings in c and d indicate the standard error.

3 Spatial-temporal features

3.1 *Statistical characteristics*

As is shown in Figs 1a and c, the overall level of EKE in the study area is relatively high, especially in the KE jet and its vicinity, and EKE shows an annual variation which is strong in summer and autumn, but weak in winter and spring, which is consistent with the conclusions of previous studies (Ji et al., 2018). The temporal correlation coefficient between mesoscale SST anomaly and SSH anomaly in the region is strongly positive, and exceeds 0.4 for most of the area that passes the significance test of 0.01 (Fig. 1b), which denotes that positive/negative SSH anomaly are more relevant to positive/negative SST anomaly, except for the area south of the KE jet, which can be expressed as the most densely packed sea surface ADT contour lines in Fig. 1a. Meanwhile, the spatial correlation coefficient of mesoscale SST anomaly and SSH anomaly fields in Fig. 1d shows an annual variation pattern of weakest in summer (June to August, <0.3) and strongest in winter (December to January in the following year, >0.5), indicating that the SSH anomaly field caused by the mesoscale eddy in summer has a relatively strong (weak) spatial correlation with the SST anomaly field in summer (winter), which is speculated to be related to the seasonal regularity of abnormal eddy activity to a certain extent.

In this paper, the average SST (SSH) anomaly within one radius from the eddy center is selected as the SST (SSH) anomaly of the eddy core, and the scatter distribution of SST anomaly and SSH anomaly within the eddy core is shown in Fig. 2. The average SSH anomaly inside the CE/AE core is basically in the range of (–60 cm to 10 cm)/(–10 cm to 50 cm), at the same time, the average SST anomaly is in the range of (–3℃ to 2℃)/(–2℃ to 3℃). The proportion of abnormal points inside the eddy core is also shown in Fig. 2. The SST anomaly roughly increases/decreases with the increase/decrease of the SSH anomaly. It can be seen that there is also an inverse phase relationship between SST anomaly and SSH anomaly associated with oceanic mesoscale eddy, and there is quite a proportion of CEs with warm-core feature and AEs with cold-core feature. During the study period, there are 313 415 CE snapshots in the study area, of which 90 295 (28.81%) correspond to positive SST anomaly and meet the condition for warm-core eddy snapshots defined in this paper. Similarly, there are 298 113AE snapshots, of which 90 780 (30.45%) correspond to negative SST anomaly and meet the condition for cold-core eddy snapshots defined in our study. The total number of CEs is larger than that of AEs, whereas the number of WCEs is smaller than CAEs, thus the proportion of abnormal eddies is higher in CAEs. Figure 2 indicates that the higher the proportion $\gamma_{\rm b}$ is, the larger the corresponding value of positive/negative temperature anomaly averaged in CE/AE core will be. It should be noted that in Fig. 2a/Fig. 2b, a small portion of the points represent positive/negative values for the average SSH anomaly within the cyclonic/anticyclonic eddy. This is largely because the eddy radius provided by the atlas is represented by a circular radius of equal area to the actual eddy range, which may not necessarily be a perfect circle, resulting in some grid points locating outside the actual eddy range are included when calculating the average SSH anomaly.

In order to make the definition method of abnormal eddy in this study more comprehensible, the evolution process of a CE that generated at (41.33°N, 155.80°E) on March 26, 2000 and lasted for 261 d with an average radius of 71.1 km and an average amplitude of 6.9 cm, and an AE that generated at (40.64°N, 165.80°E) on October 24, 2002 and lasted for 157 d with an average radius of 73.4 km and an average amplitude of 6.8 cm were analyzed. Figure 3 shows the evolution of the mean SST anomaly ($T'_{\rm in}$) and proportion γ_b within the CE and AE cores with the development of the eddy from its generation to death, respectively. According to the evaluation conditions in this study ($T'_{\rm in} > 0$℃), there are three times converting to WCE during the CE lifetime in Fig. 3a: Days 29 to 59, Days 84 to 102, and Days 146 to 178. In Fig. 3b, considering the evaluation conditions of conversion to CAE ($T'_{\rm in} < 0$℃), the AE is transformed into CAE four times during its lifetime: Days 20 to 29, Days 41 to 67, Days 102 to 113, and Days 141 to 157. Abnormal eddy snapshots are consistence with relative large proportion $\gamma_{\rm b}$. It is obvious in Fig. 3 that an eddy may turn into an abnormal eddy more than once during its life cycle and maintain the abnormal signal for several days.

3.2 *Spatial features*

Statistical analysis is conducted on WCEs, CAEs, CCEs, and

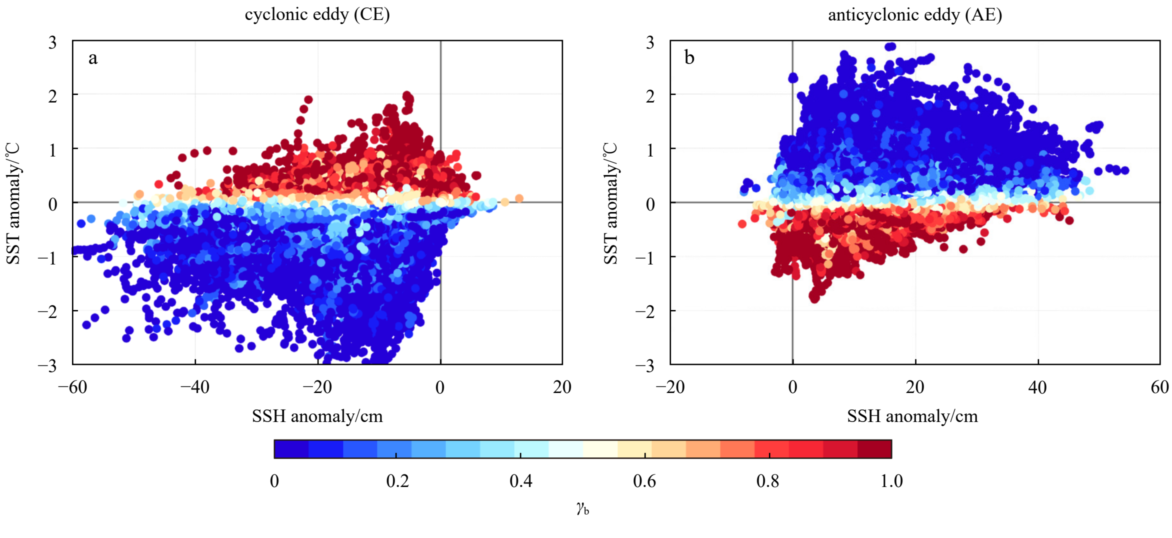

Fig. 2. Scatter plots of sea surface height (SSH) anomaly and sea surface temperature (SST) anomaly averaged inside the eddy core corresponding to CE (a) and AE (b). The color of scatter plots denotes the proportion $\gamma_{\rm b}$ of abnormal points within one radius from the eddy center.

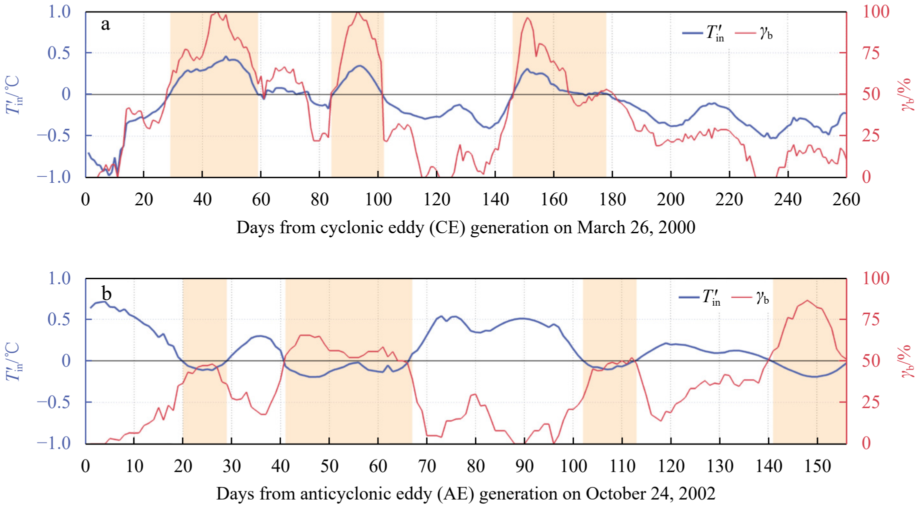

Fig. 3. The evolution process of the average T'_{in} (blue curves) and proportion γ_{b} (red curves) inside the eddy core during the lifetime of a CE (a) and an AE (b). The orange shadings mark the abnormal eddy duration periods according to the definition conditions in this study.

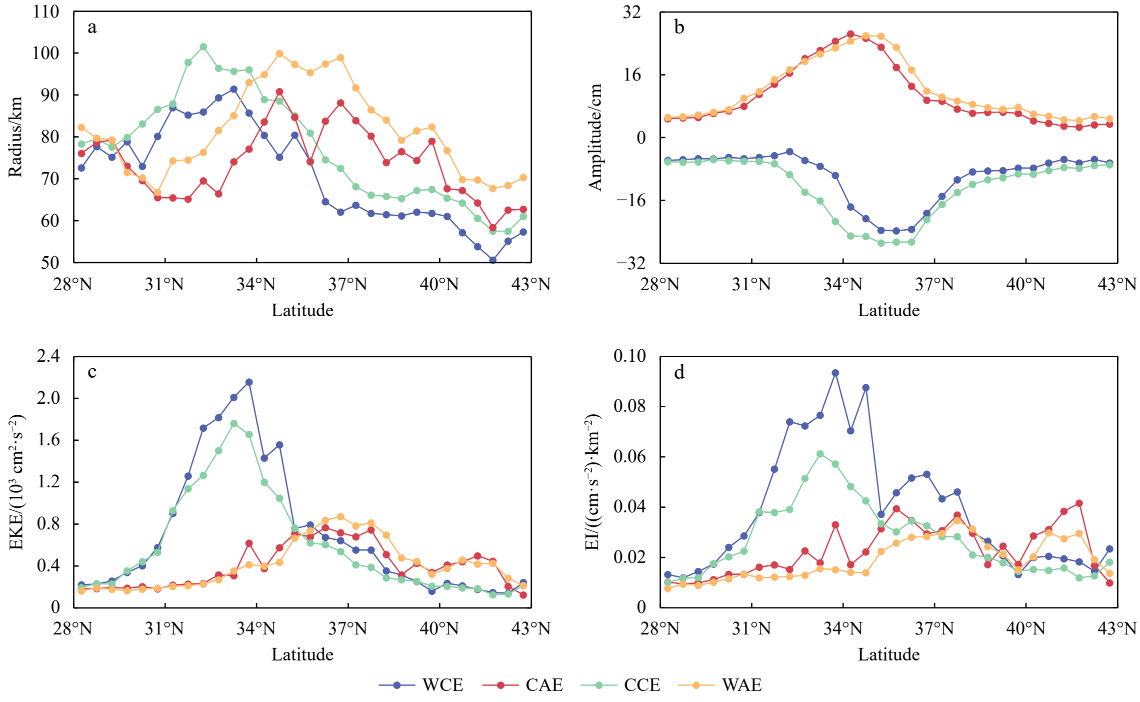

Fig. 4. The distribution of zonal average radius (a), amplitude (b), eddy kinetic energy (EKE, c) and EKE intensity (EI, d) for each type of eddies in 0.5°-width latitudinal bands. WCE, warm cyclonic eddy; CAE, cold anticyclonic eddy; CCE, cold cyclonic eddy; WAE, warm anticyclonic eddy.

WAEs in the study area during 1993 to 2019 to obtain the spatial distribution of characteristics like radius, amplitude, maximum rotational velocity, and proportion of each type of eddies in the corresponding polarity eddies (shown in Fig. 4). It is clear in Fig. 4a that the maximum values of radius for WCEs/CCEs appear at latitudes near the 32°N/33°N, while those for CAEs/WAEs appear at slightly higher latitudes in the range of 35°N to 37°N, which are also around the KE jet (defined as 35°N thereafter according to contours in Fig. 1a). At most latitudes, the zonally-average radius of both WCEs and CAEs is always smaller than that of the corresponding conventional eddies, whereas the latitudes at which the maximum values occur are basically the same no matter whether the eddies are abnormal or not.

Figure 4b shows that the zonally-average amplitude for four types of eddies also has an extreme value at latitudes near the KE jet. By combining the latitudinal distribution features of zonally-average radius (Fig. 4a) with that of amplitude (Fig. 4b) for four types of eddies, it can be seen that the average amplitude of CEs is larger and the average radius is smaller than AEs in the north of the KE jet. On the contrast, the average amplitude of CEs is smaller and the average radius is larger than AEs in the south of the KE jet. The latitudinal variation of average amplitude for abnormal eddies is similar with that of normal eddies, except the value of amplitude for abnormal eddies is slightly smaller than that of corresponding normal eddies.

Figure 4c shows the zonal average of EKE for four types of eddies based on the EKE information for each eddy snapshot provided by the eddy dataset, also revealing an asymmetry between the two sides of KE jet. The average EKE of AEs is higher in the area north of 35°N than south of it, with the highest values near 37°N, reaching approximately 800 $\mathrm{cm}^2/\mathrm{s}^2$. On the other hand, CEs exhibit higher EKE south of 35°N, with the highest values near 33.5°N, especially WCEs, reaching up to 2 200 $\mathrm{cm}^2/\mathrm{s}^2$. Based on the EKE and radius information, the EKE intensity (EI) of eddies is calculated by dividing the EKE of each eddy by its area, which can be used to measure the intensity of the eddy. It can be indicated in Fig. 4d that WCEs have the strongest EI among all four types of eddies across most latitudes in the study area. In area south of the KE jet, high levels of EKE result in a peak near 33.5°N (0.096 $(\mathrm{cm}^2 \cdot \mathrm{s}^{-2})/\mathrm{km}^2$), whereas smaller radius lead to a secondary peak near 37°N (0.054 $(\mathrm{cm}^2 \cdot \mathrm{s}^{-2})/\mathrm{km}^2$) in the north of the KE jet. Overall, both types of CEs have higher intensity in the south of the KE jet, whereas both types of AEs have larger intensity in the north. Besides, when considering the same polarity, abnormal eddies generally have a higher EI than normal eddies at the same latitude due to the smaller size, which means a more concentrated energy.

3.3 *Temporal variation*

The annual variation of the occurrence frequency of four types of eddies during the selected period in the study area is shown in Fig. 5. It is clear that the proportion of abnormal eddies is larger in the area south of the KE jet, which can reach up to 50% at latitudes around 30°N in specific seasons (Figs 5a and b). Dong et al. (2017) indicated that the temperature anomaly of mesoscale eddies was shown as subsurface intensified structures on the south side of the KE jet, whereas near-surface intensified structures on the north side, which can explain such higher proportion of eddies with abnormal SST anomaly in the south flank of KE jet. It can also be found that in most areas, the proportion of abnormal eddies is highest in summer and lowest in winter (Figs 5a and b), except for CAEs south of 32°N, of which the seasonal variation is not significant. The seasonal discrepancy of the proportion, especially for WCEs south of the KE jet and CAEs near the KE jet, is most pronounced.

Figures 5c and d show that the occurrence numbers of conventional CCEs and WAEs in the KE region are both highest in boreal winter and spring, whereas lowest in summer and autumn. However, the number and proportion of abnormal WCEs reach the highest in July (about 400 a^{-1}, 37%) and the lowest in February (about 150 a^{-1}, 15%). Whereas for CAEs, the number and proportion reach the highest in June (about 340 a^{-1}, 35%) and the lowest in December (about 170 a^{-1}, 18%). The seasonal variation of proportion of abnormal eddies could explain why the spatial correlation between mesoscale SST anomaly and SSH anomaly in the study area shows a seasonal cycle of lowest in summer and highest in winter as is shown in Fig. 1d, and the latitudinal variation of proportion could explain why the temporal correlation coefficient is smaller in area south of the KE jet as is shown in Fig. 1b. Based on Figs 5a–d, it can be concluded that for either type of abnormal eddies in the study area, its proportion is generally higher in summer than in winter, which indicates that the marine environment in the study area during summer is more favorable for the formation and maintenance of abnormal

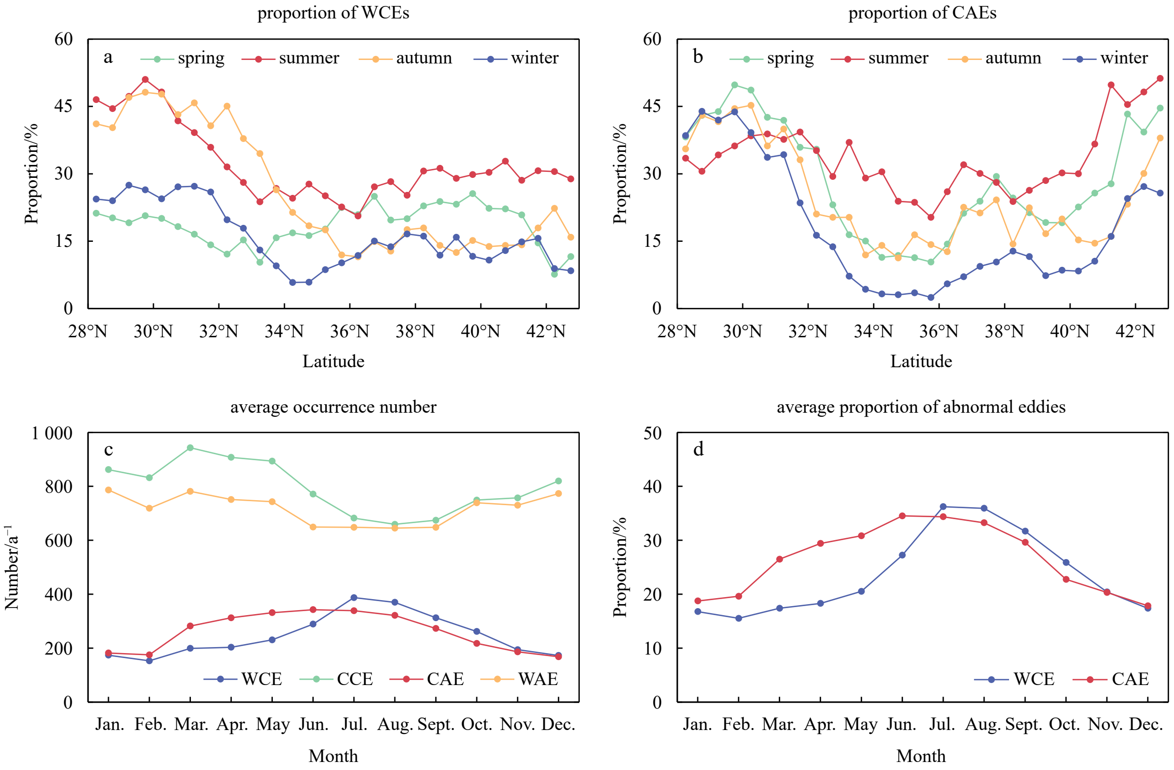

Fig. 5. Seasonal variation of the occurrence frequency of four types of eddies. a. Proportion of WCEs in all cyclonic eddies in each 0.5° latitudinal bands in four seasons; b. the same with a, but for CAEs in all anticyclonic eddies; c. average occurrence numbers for four types of eddies in each month; d. average proportion of abnormal eddies in all eddies in each month. WCE, warm cyclonic eddy; CAE, cold anticyclonic eddy; CCE, cold cyclonic eddy; WAE, warm anticyclonic eddy.

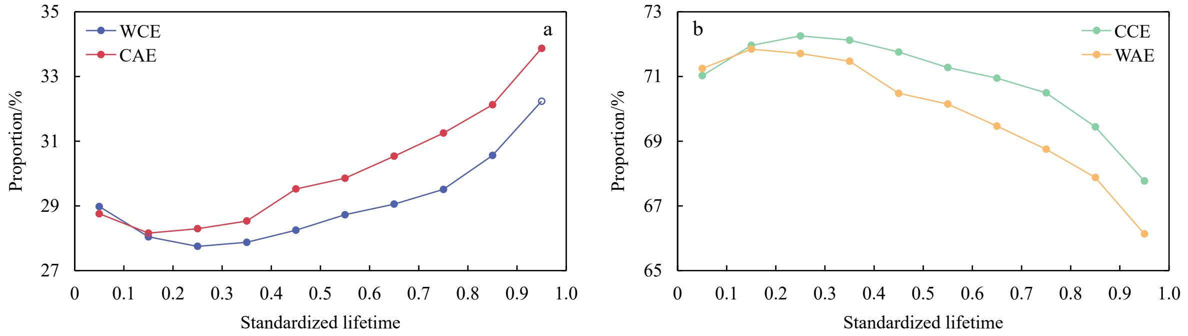

Fig. 6. The proportion of abnormal eddies (a) and normal eddies (b) in total eddies with corresponding polarity. WCE, warm cyclonic eddy; CAE, cold anticyclonic eddy; CCE, cold cyclonic eddy; WAE, warm anticyclonic eddy.

eddies.

In this study, four types of eddies in the study area are temporally standardized according to their respective duration time. As can be seen in Fig. 6a, a larger proportion of CAEs in all AEs than that of WCEs in all CEs occurs during almost whole duration of the eddy lifetime, except for the beginning stage. Moreover, the existence proportion of WCEs/CAEs in all CEs/AEs decreases from about 29% to 28% during the 0–0.3 standardized survival period and then increases steadily to 34%/32% before the eddy extinction. In contrast, the proportion of CCEs/WAEs in all CEs/AEs increases firstly and then decreases steadily before eddy disappears (Fig. 6b). During the last 0.3 standardized lifetime of the eddy, the proportion of WCEs/CAEs increases rapidly from 29.4%/31.2% to 32.3%/34.0%, which accounts for 67%/47% of the difference between its maximum and minimum values. The rapid increase in the proportion of abnormal eddies during the decaying stage of eddies can be attributed to the enlargement of eddy radius, which leads to the absorption of surrounding warm/cold seawater (Sun et al., 2019a) or various instability (Sun et al., 2021).

Due to the above characteristics of abnormal eddies, there are spatial differences between the north and south regions divided by the KE jet, as well as significant seasonal differences between summer and winter. Figure 7 shows the *T-S* diagram of the study area for different seasons on both sides of 35°N. It is evident that there are significant differences in the marine environment between the north and south regions. The seawater south of 35°N has higher temperature, greater salinity, and denser stratification than the seawater north of it. In the same region, the marine environment near the surface also exhibits significant differences between the winter and summer. This will inevitably lead to spatiotemporal differences in the characteristics of abnormal eddies in the study area.

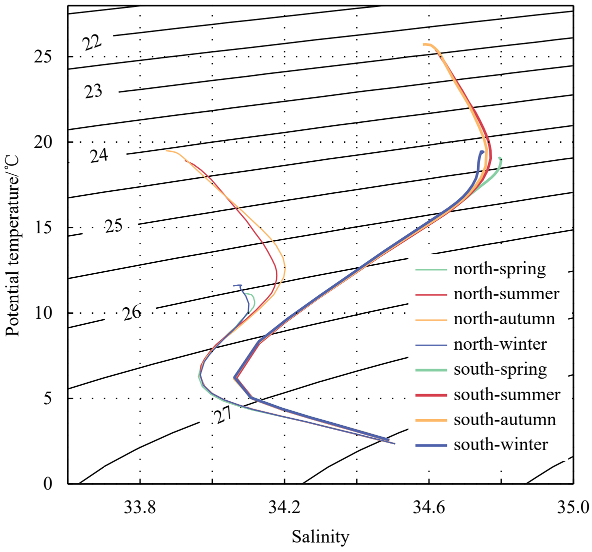

Fig. 7. Average potential temperature and salinity characteristics in study area for four seasons. The black contour lines represent potential density, the thin colored lines represent the region north of 35°N, while the thick ones represent the region south of it.

4 Analysis of composite structures

4.1 *Sea surface structures*

In order to compare the difference in spatial structures between abnormal eddies and normal eddies, the pattern of SST anomaly and SSH anomaly for four types of eddies within twice the radius are composited, as is shown in Fig. 8. Obviously, the WCE (Fig. 8a) has a negative SSH anomaly (with an extreme value of about −14.2 cm) and a positive SST anomaly (with an extreme value of about 0.22℃) composite structure, with the warm core locating about 0.8 times of radius east of the eddy center (IAE = −0.63). Contrastively, the CCE (Fig. 8b) has a more significant negative SSH anomaly (with a larger amplitude of about −17.0 cm), of which the large positive IAE value (0.98) denotes a negative and quasi-monopolar SST anomaly pattern.

The composite structure of CAE (Fig. 8c) has a weaker positive SSH anomaly (with an extreme value of about 10.8 cm) than the other three types of eddies and an abnormal SST anomaly feature (IAE = −0.52), with the cold core locating south of the eddy center. Whereas the composite structure of WAE (Fig. 8d) has a positive SSH anomaly (about 15.2 cm) and a warm-core feature (IAE = 0.85), which is less monopolar than that of CCE. In summary, in addition to the differences in SST anomaly structure, both types of CEs have a larger amplitude than AEs, while for eddies with the same polarity, abnormal eddies have a smaller amplitude and weaker SST anomaly than normal eddies, which is consistent with the characteristic differences shown in Figs 3a and b. This may be due to the fact that abnormal eddies have the highest proportion during the decaying phase of eddies, as is shown in Fig. 6a, when the amplitude and radius of the eddies are both smaller compared to the mature phase.

4.2 *Vertical structures*

The three-dimensional structures of temperature anomaly and V_g anomaly for four types of eddies are calculated and com-

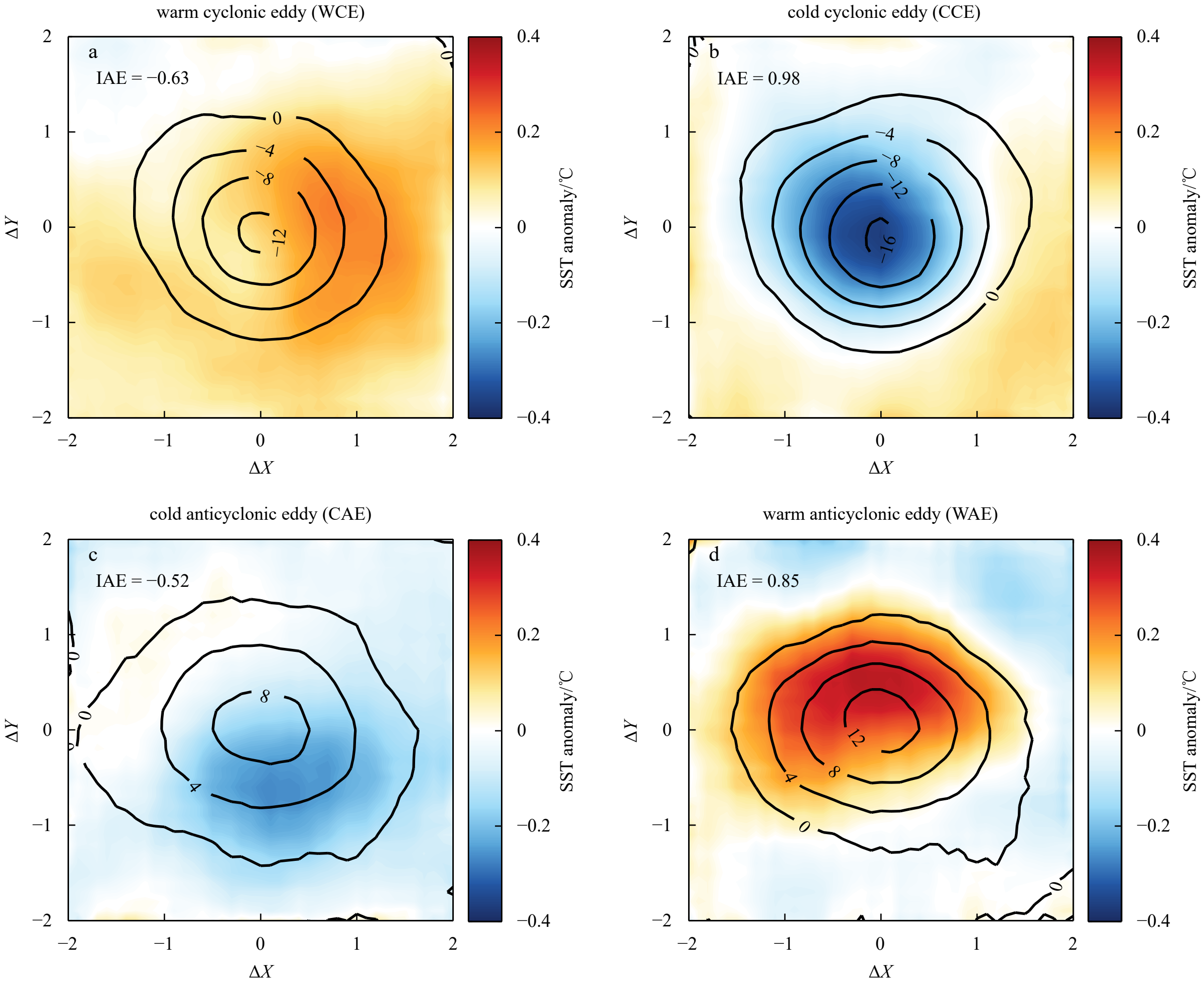

Fig. 8. Composite sea surface temperature (SST) anomaly (color shading) and sea surface height (SSH) anomaly (contours, unit: cm) of WCEs (a), CCEs (b), CAEs (c) and WAEs (d). IAE, index of abnormal eddy.

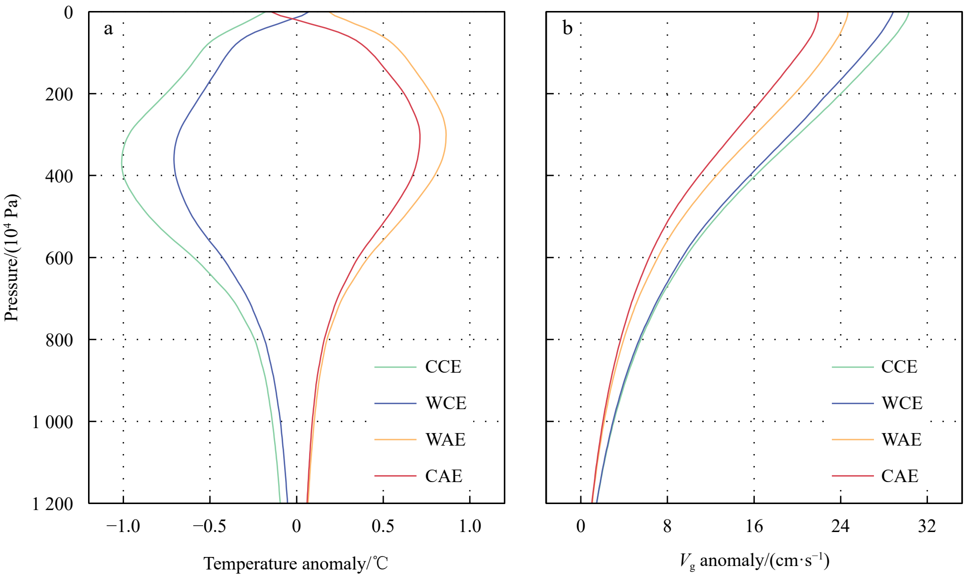

Fig. 9. Vertical profiles of the temperature anomaly averaged within the radius (a) and maximum V_g anomaly on each level of the composite eddy structures (b). WCE, warm cyclonic eddy; CAE, cold anticyclonic eddy; CCE, cold cyclonic eddy; WAE, warm anticyclonic eddy.

posited based on the T/S field. The vertical profiles of the temperature anomaly and the V_g anomaly of the composite eddy structures are illustrated in Fig. 9. Figure 9a shows that the CCEs/WAEs result in cold/warm anomaly at the layers from sea surface to at least 1 200 m depth, whereas the WCEs/CAEs present an abnormal warm/cold feature at the sea surface, which gradually weakens with the depth, converts to a common cold/warm anomaly at about 30 m and strengthens with the depth. The average temperature anomaly of the abnormal WCEs/CAEs on each layer is also weaker than that of normal CCEs/WAEs, with a difference up to 0.28℃/0.15℃ at about 360 m/300 m depth. Regardless of whether it is abnormal or not, the maximum value of temperature anomaly inside CEs occurs at about 360 m, which is –1.05℃/–0.73℃, whereas the average profile of AEs has a maximum value of 0.85℃/0.72℃ at a shallower layer (about 300 m).

According to Fig. 9b, the maximum tangential velocity around the eddy center is largest at the sea surface, with that of the CCEs/WAEs reaching (28.5 cm/s)/(24.8 cm/s), and then decreases with depth. The maximum V_g anomaly of the CCEs is 1.5 cm/s faster than the WCEs at the sea surface, while that of WAEs is 3.3 cm/s faster than the CAEs. The difference between WCEs/CAEs and CCEs/WAEs decreases with the depth, until about 600 m/900 m depth, respectively. It is also obvious in Fig. 9b that the priority for rotational velocity of cyclonic eddies over anticyclonic eddies could last from sea surface to layers at least 1 200 m.

In order to exhibit the vertical structures for all types of eddies more intuitionally, Fig. 10 shows the east-west sections across the eddy center of the composite structure for CCEs, WCEs, WAEs, and CAEs. It can be seen that the rotational velocity near the eddy center from sea surface to deep layer is close to 0 cm/s for all types of oceanic eddies. Compared with CCEs, the rotating velocity of WCEs is slightly weaker (Figs 10a and b), whereas there is no significant difference between the tangential velocity sections of CAEs and WAEs (Figs 10c and d).

It can be clearly seen from Fig. 10 that the temperature anomaly induced by CEs and AEs are mainly confined within one radius from the eddy center in the horizontal direction, regardless of whether it is abnormal or not, whereas the temperature anomaly with opposite sign and small value is presented in the range of 1.2–2 times the radius from the center. In the vertical direction, the signal of local seawater temperature anomaly caused by the eddy can extend to the water layer at least 1 200 m, meanwhile, the abnormal temperature anomaly signal for WCEs (CAEs) is limited to the near sea surface.

Consistent with the result in Fig. 9, the extreme value of temperature anomaly for WCEs (CCEs) also appears at around 360 m, with an amplitude of about –1.6℃ (–2.4℃). The core of CAEs (WAEs) is shallower, with an extreme value of about 1.3℃

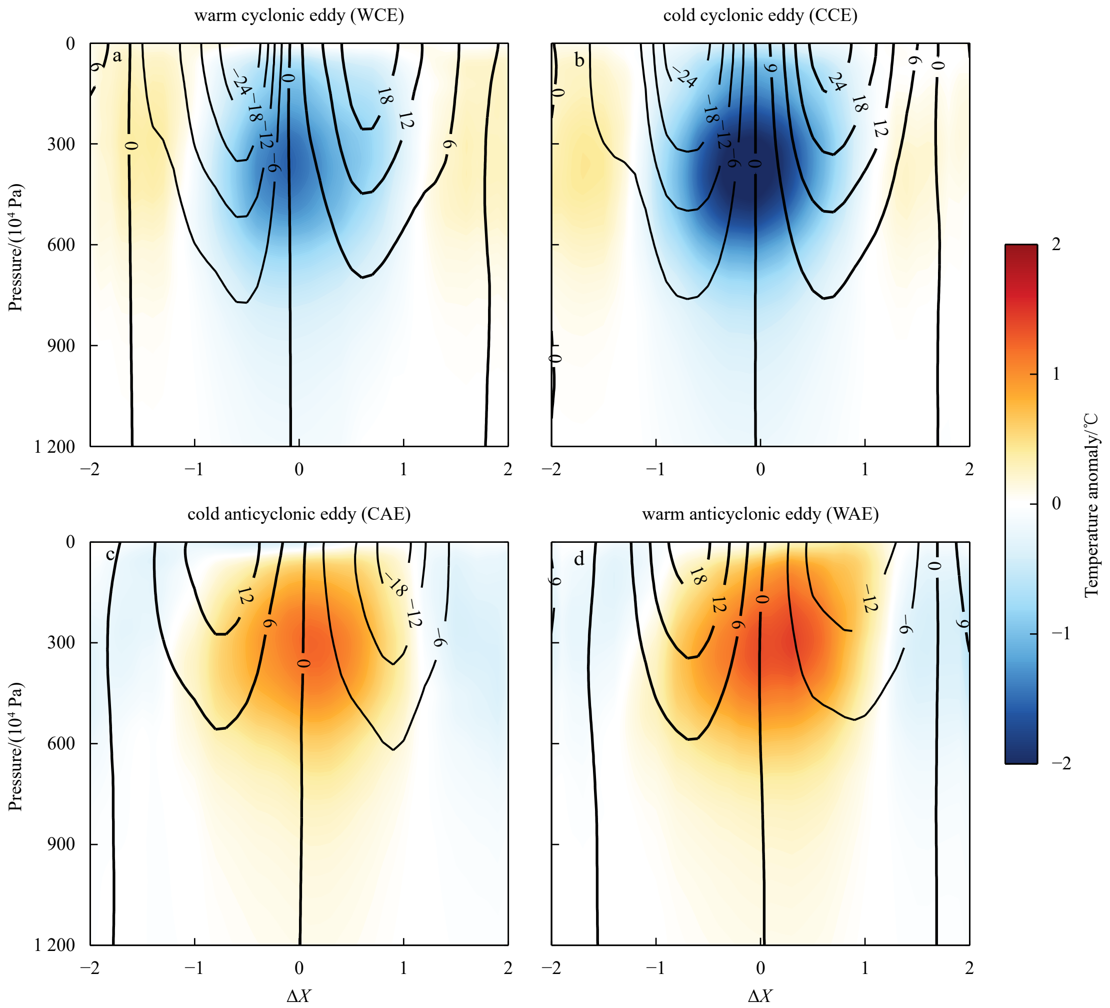

Fig. 10. West-east sections of temperature anomaly (color shading) and geostrophic velocity anomaly (contours, unit: cm/s) across the center of composite WCEs (a), CCEs (b), CAEs (c) and WAEs (d).

(1.6℃) in temperature anomaly that appears at about 300 m depth. In a word, the amplitude of composite temperature anomaly structures for abnormal eddies is smaller than that for normal eddies with the same polarity. However, whether abnormal or not has little influence on the depth of the extreme value, and the inconsistency in sign caused by abnormal eddy is only reflected in the temperature anomaly near the sea surface.

5 Summary and discussion

According to the definition method in this paper, and based on the mesoscale eddy information provided by the global eddy trajectory atlas, satellite altimetric data, and remote sensing data, the WCEs and CAEs are selected in the KE region in the North Pacific Ocean. The characteristics of WCEs and CAEs like radius, amplitude, EKE, and EKE intensity are statistically analyzed and compared with those for CCEs and WAEs in spatial distribution. The results show that the all these characteristics exhibit asymmetry on the north and south sides of the KE jet without considering whether it is abnormal or not. On the north side of the jet, the AE has a larger radius, smaller amplitude, larger EKE and EKE density. Whereas on the south side of the KE jet, it is the CE that has a larger radius, smaller amplitude, and larger EKE intensity instead. The average radius and amplitude of abnormal eddies is slightly smaller than that of conventional ones, whereas the higher EKE and smaller size result in the more concentrated EKE of abnormal eddies.

The proportion of abnormal eddies among the total eddies also exhibits asymmetry, especially for WCEs. The proportion also shows significant seasonal variations, particularly for WCEs south of the KE jet and CAEs near the KE jet. In contrast to the overall seasonal variation pattern of all eddies, the number and proportion of abnormal eddies are generally highest in summer and lowest in winter. These spatial and temporal differences are largely related to the north-south discrepancy and seasonal variation in the marine environment, but the specific physical mechanisms require further discussion to be determined.

According to the standardized lifecycle of eddies, it is indicated that the proportion of abnormal eddies rapidly increases during the decaying phase. This largely results in the WCEs/CAEs having smaller average radius, amplitude, SST anomaly and SSH anomaly compared to CCEs/WAEs. Additionally, abnormal eddies do not only have smaller SST anomaly than conventional ones at the sea surface, but also exhibit smaller amplitude of temperature anomaly and V_g anomaly at various depths beneath the surface. Besides, vertical structures indicate that the temperature anomaly is not limited to the sea surface, levels above the depth of about 30 m also shows an abnormal signal.

This study reveals the spatiotemporal characteristics of abnormal eddies in the highly active KE region of the North Pacific Ocean. It indicates that there is a certain relationship between the activity features of abnormal eddies and spatiotemporal evolution of the marine environment. However, the specific physical mechanisms underlying this relationship require further exploration and research.

Acknowledgements

The altimetric Mesoscale Eddy Trajectories Atlas (META3.1exp DT) was produced by SSALTO/DUACS and distributed by AVISO+ (https://aviso.altimetry.fr) with support from CNES, in collaboration with IMEDEA (DOI: 10.24400/527896/a01-2021.001 for the META3.1exp DT allsat version and 10.24400/527896/a01-2021.002 for the MET3.1exp DT twosat version.

References

Castellani M. 2006. Identification of eddies from sea surface temperature maps with neural networks. International Journal of Remote Sensing, 27(8): 1601–1618, doi: 10.1080/01431160500462170

Chaigneau A, Le Texier M, Eldin G, et al. 2011. Vertical structure of mesoscale eddies in the eastern South Pacific Ocean: A composite analysis from altimetry and Argo profiling floats. Journal of Geophysical Research: Oceans, 116(C11): C11025, doi: 10.1029/2011JC007134

D'Alimonte D. 2009. Detection of mesoscale eddy-related structures through ISO-SST patterns. IEEE Geoscience and Remote Sensing Letters, 6(2): 189–193, doi: 10.1109/LGRS.2008.2009550

Desbiolles F, Alberti M, Hamouda M E, et al. 2021. Links between sea surface temperature structures, clouds and rainfall: study case of the Mediterranean Sea. Geophysical Research Letters, 48(10): e2020GL091839, doi: 10.1029/2020GL091839

Dilmahamod A F, Aguiar-González B, Penven P, et al. 2018. SIDDIES corridor: A major east-west pathway of long-lived surface and subsurface eddies crossing the subtropical South Indian Ocean. Journal of Geophysical Research: Oceans, 123(8): 5406–5425, doi: 10.1029/2018JC013828

Dong D, Brandt D, Chang P, et al. 2017. Mesoscale eddies in the northwestern Pacific Ocean: Three-dimensional eddy structures and heat/salt transports. Journal of Geophysical Research: Oceans, 122(12): 9795–9813, doi: 10.1002/2017JC013303

Everett J D, Baird M E, Oke P R, et al. 2012. An avenue of eddies: Quantifying the biophysical properties of mesoscale eddies in the Tasman Sea. Geophysical Research Letters, 39(16): L16608, doi: 10.1029/2012GL053091

Fernandes A, Nascimento S. 2006. Automatic water eddy detection in SST maps using random ellipse fitting and vectorial fields for image segmentation. In: Proceedings of the 9th International Conference on Discovery Science. Barcelona, Spain: Springer, 77–88, doi: 10.1007/118933318_11

Frenger I, Münnich M, Gruber N, et al. 2015. Southern Ocean eddy phenomenology. Journal of Geophysical Research: Oceans, 120(11): 7413–7449, doi: 10.1002/2015JC011047

Gaube P, Chelton D B, Samelson R M, et al. 2015. Satellite observations of mesoscale eddy-induced Ekman pumping. Journal of Physical Oceanography, 45(1): 104–132, doi: 10.1175/JPO-D-14-0032.1

Itoh S, Yasuda I. 2010a. Water mass structure of warm and cold anticyclonic eddies in the western boundary region of the subarctic North Pacific. Journal of Physical Oceanography, 40(12): 2624–2642, doi: 10.1175/2010JPO4475.1

Itoh S, Yasuda I. 2010b. Characteristics of mesoscale eddies in the Kuroshio-Oyashio Extension region detected from the distribution of the sea surface height anomaly. Journal of Physical Oceanography, 40(5): 1018–1034, doi: 10.1175/2009JPO4265.1

Ji Jinlin, Dong Changming, Zhang Biao, et al. 2017. An oceanic eddy statistical comparison using multiple observational data in the Kuroshio Extension region. Acta Oceanologica Sinica, 36(3): 1–7, doi: 10.1007/s13131-016-0882-1

Ji Jinlin, Dong Changming, Zhang Biao, et al. 2018. Oceanic eddy characteristics and generation mechanisms in the Kuroshio Extension region. Journal of Geophysical Research: Oceans, 123(11): 8548–8567, doi: 10.1029/2018JC014196

Kouketsu S, Kaneko H, Okunishi T, et al. 2016. Mesoscale eddy effects on temporal variability of surface chlorophyll *a* in the Kuroshio Extension. Journal of Oceanography, 72(3): 439–451, doi: 10.1007/s10872-015-0286-4

Liu Yingjie, Zheng Quanan, Li Xiaofeng. 2021. Characteristics of global ocean abnormal mesoscale eddies derived from the fusion of sea surface height and temperature data by deep learning. Geophysical Research Letters, 48(17): e2021GL094772, doi: 10.1029/2021GL094772

Lv Mingkun, Wang Fan, Li Yuanlong, et al. 2022. Structure of sea surface temperature anomaly induced by mesoscale eddies in the North Pacific Ocean. Journal of Geophysical Research: Oceans, 127(3): e2021JC017581, doi: 10.1029/2021JC017581

Ma Jing, Xu Haiming, Dong Changming, et al. 2015. Atmospheric responses to oceanic eddies in the Kuroshio Extension region. Journal of Geophysical Research: Atmospheres, 120(13): 6313–6330, doi: 10.1002/2014JD022930

Mathis J T, Pickart R S, Hansell D A, et al. 2007. Eddy transport of organic carbon and nutrients from the Chukchi shelf: impact on the upper halocline of the western Arctic Ocean. Journal of Geophysical Research: Oceans, 112(C5): C05011, doi: 10.1029/2006JC003899

Ni Qinbiao, Zhai Xiaoming, Jiang Xuemin, et al. 2021. Abundant cold anticyclonic eddies and warm cyclonic eddies in the global ocean. Journal of Physical Oceanography, 51(9): 2793–2806, doi: 10.1175/JPO-D-21-0010.1

Ni Qinbiao, Zhai Xiaoming, Yang Zhibin, et al. 2023. Generation of cold anticyclonic eddies and warm cyclonic eddies in the tropical oceans. Journal of Physical Oceanography, 53(6): 1485–1498, doi: 10.1175/JPO-D-22-0197.1

Pegliasco C, Delepoulle A, Mason E, et al. 2022. META3.1exp: a new global mesoscale eddy trajectory atlas derived from altimetry. Earth System Science Data, 14(3): 1087–1107, doi: 10.5194/essd-14-1087-2022

Qiu Bo, Chen Shuiming, Schneider N. 2017. Dynamical links between the decadal variability of the Oyashio and Kuroshio extensions. Journal of Climate, 30(23): 9591–9605, doi: 10.1175/JCLI-D-17-0397.1

Renault L, Masson S, Oerder V, et al. 2019. Disentangling the mesoscale ocean-atmosphere interactions. Journal of Geophysical Research: Oceans, 124(3): 2164–2178, doi: 10.1029/2018JC014628

Shan Xuan, Jing Zhao, Gan Bolan, et al. 2020a. Surface heat flux induced by mesoscale eddies cools the Kuroshio-Oyashio Extension region. Geophysical Research Letters, 47(1): e2019GL086050, doi: 10.1029/2019GL086050

Shan Xuan, Jing Zhao, Sun Bingrong, et al. 2020b. Impacts of ocean current-atmosphere interactions on mesoscale eddy energetics in the Kuroshio Extension region. Geoscience Letters, 7(1): 3, doi: 10.1186/s40562-020-00152-w

Sun Wenjin, Dong Changming, Tan Wei, et al. 2019a. Statistical characteristics of cyclonic warm-core eddies and anticyclonic cold-core eddies in the North Pacific based on remote sensing data. Remote Sensing, 11(2): 208, doi: 10.3390/rs11020208

Sun Shuangwen, Fang Yue, Zu Yongcan, et al. 2020. Seasonal characteristics of mesoscale coupling between the sea surface temperature and wind speed in the South China Sea. Journal of Climate, 33(2): 625–638, doi: 10.1175/JCLI-D-19-0392.1

Sun Bowen, Li Baofu, Yan Jingyu, et al. 2022. Seasonal variation of atmospheric coupling with oceanic mesoscale eddies in the North Pacific Subtropical Countercurrent. Acta Oceanologica Sinica, 41(10): 109–118, doi: 10.1007/s13131-022-2022-4

Sun Wenjin, Liu Yu, Chen Gengxin, et al. 2021. Three-dimensional properties of mesoscale cyclonic warm-core and anticyclonic cold-core eddies in the South China Sea. Acta Oceanologica Sinica, 40(10): 17–29, doi: 10.1007/s13131-021-1770-x

Sun Bowen, Liu Chuanyu, Wang Fan. 2019b. Global meridional eddy heat transport inferred from Argo and altimetry observations. Scientific Reports, 9(1): 1345, doi: 10.1038/s41598-018-38069-2

Xu Quanqian, Xu Haiming, Ma Jing. 2018. Air-sea relationship associated with mesoscale oceanic eddies over the subtropical North Pacific in summer. Chinese Journal of Atmospheric Sciences (in Chinese), 42(6): 1191–1207, doi: 10.3878/j.issn.1006-9895.1711.17180

Yang Haiyuan, Qiu Bo, Chang Ping, et al. 2018. Decadal variability of eddy characteristics and energetics in the Kuroshio Extension: Unstable versus stable states. Journal of Geophysical Research: Oceans, 123(9): 6653–6669, doi: 10.1029/2018JC014081

Yang Guang, Yu Weidong, Yuan Yeli, et al. 2015. Characteristics, vertical structures, and heat/salt transports of mesoscale eddies in the southeastern tropical Indian Ocean. Journal of Geophysical Research: Oceans, 120(10): 6733–6750, doi: 10.1002/2015JC011130

Yang Guangbing, Zheng Quanan, Xiong Xuejun. 2023. Subthermocline eddies carrying the Indonesian Throughflow water observed in the southeastern tropical Indian Ocean. Acta Oceanologica Sinica, 42(5): 1–13, doi: 10.1007/s13131-022-2085-2

Yao Hengkai, Ma Chao, Jing Zhao, et al. 2023. On the vertical structure of mesoscale eddies in the Kuroshio-Oyashio Extension. Geophysical Research Letters, 50(24): e2023GL105642, doi: 10.1029/2023GL105642

Yu Fangjie, Wang Zeyuan, Liu Shuai, et al. 2021. Inversion of the three-dimensional temperature structure of mesoscale eddies in the Northwest Pacific based on deep learning. Acta Oceanologica Sinica, 40(10): 176–186, doi: 10.1007/s13131-021-1841-z

Zu Yongcan, Sun Shuangwen, Zhao Wei, et al. 2019. Seasonal characteristics and formation mechanism of the thermohaline structure of mesoscale eddy in the South China Sea. Acta Oceanologica Sinica, 38(4): 29–38, doi: 10.1007/s13131-018-1222-4